Journal of Materials Chemistry C

ROYAL SOCIETY OF CHEMISTRY

PAPER

View Article Online
View Journal | View Issue

Cite this: J. Mater. Chem. C, 2024, 12, 6479

Achieving outstanding energy storage behaviors *via* combinatorial optimization design in BNT-based relaxor ferroelectric ceramics under medium–low electric fields

Jian Yang,[a] Xiaolong Zhu,[a] Haotian Wang,[a] Yixiao Zhang,[a] Pengfei Guan,[a] Shiguang Yan[b] and Ming Zheng *[ab]

As the development of electronic components has become highly integrated and diversified, dielectric ceramic energy storage capacitors have attracted wide attention due to their high-power density, low cost and ability to operate at high temperatures. In this work, we have designed $(0.8 - x)Bi_{0.5}Na_{0.5}TiO_3$–$0.2BaZr_{0.3}Ti_{0.7}O_3$–$xNaNbO_3$ (abbreviated as $(0.8 - x)$BNT–0.2BZT–xNN) lead-free relaxor ferroelectric ceramics and successfully optimized the energy storage performance by synergistically modifying critical factors affecting energy storage properties. The 0.7BNT–0.2BZT–0.1NN ceramic achieved high maximum polarization (P_{max} = 42.1 μC cm^{-2}), extremely low remnant polarization, recoverable energy storage density (W_{rec} = 3.53 J cm^{-3}), efficiency (η = 93.5%) and W_{rec}/E = 160.45 J (kV m^{-2}) under a medium–low electric field (E = 220 kV cm^{-1}). The simultaneous achievement of high energy storage density and efficiency under lower electric fields is due to the expansion of the octahedral framework facilitated by Ba^{2+} and Zr^{4+}, which promotes ion displacement. $NaNbO_3$ can further improve relaxor behaviors, compensating for polarization losses caused by relaxation and enhancing breakdown field strength. Furthermore, it also exhibits excellent electric field stability (30–220 kV cm^{-1}, $\Delta\eta < 0.7\%$), thermal stability (20–140 °C, $\Delta W_{rec} < 7.2\%$), and frequency stability (1–100 Hz, $\Delta W_{rec} < 5.3\%$). This work provides an option for the selection of dielectric capacitors under limited electric field conditions.

Received 29th February 2024,
Accepted 4th April 2024

DOI: 10.1039/d4tc00818a

rsc.li/materials-c

1. Introduction

Energy storage technologies have been an indispensable topic for social development and progress. With the trend of electronic devices moving towards portability, miniaturization, and stabilization, the development of energy storage devices with small volume, low cost, wide operating temperature, and excellent performance is crucial. Ceramic-based dielectric capacitors, characterized by high power density, a wide operating temperature range, controllable and coordinated performance, and long cycle life, have become ideal for future pulse power systems.[1–4]

The energy storage density of dielectric capacitors remains relatively low, still exhibiting a certain gap compared to batteries and electrochemical capacitors. Therefore, enhancing the energy storage density of dielectric capacitors has become an important challenge. The energy storage properties of dielectric capacitors can be evaluated using the following formulas:[5–7]

$$W_{tot} = \int_0^{P_{max}} E\mathrm{d}P$$

$$W_{rec} = \int_{P_r}^{P_{max}} E\mathrm{d}P$$

$$\eta = \frac{W_{rec}}{W_{tot}} \times 100\%$$

where W_{tot}, W_{rec}, and η represent the total energy density, recoverable energy density, and efficiency, respectively. P_{max}, P_r, and E represent the maximum polarization, remnant polarization, and electric field, respectively. From the above formulas, it can be inferred that achieving high energy storage density in dielectric ceramic materials requires high P_{max}, low P_r, and high breakdown field strength (E_b). For instance, Chen *et al.*[8] introduced $CaTi_{0.5}Zr_{0.5}O_3$ into the $Bi_{0.5}Na_{0.5}TiO_3$–$NaNbO_3$ matrix, which significantly altered the grain size and conductivity, leading to an increase in the E_b. Ultimately, BNT–NN/xCZT composites with x = 7 wt% achieved optimal energy storage properties (W_{rec} = 4.93 J cm^{-3}, η = 93.3%) at 410 kV cm^{-1}. Zhang

[a] School of Materials Science and Physics, China University of Mining and Technology, Xuzhou 221116, China. E-mail: zhengm@mail.ustc.edu.cn
[b] Key Laboratory of Inorganic Functional Materials and Devices, Shanghai Institute of Ceramics, Chinese Academy of Sciences, Shanghai 200050, China

et al.[9] induced defect dipoles and reduced oxygen vacancy concentrations in $Sr_2NaNb_5O_{15}$ through the doping of CuO. A high W_{rec} of 4.17 J cm^{-3} and an η of 89.5% are achieved under a medium electric field (~350 kV cm^{-1}). Li *et al.*[10] introduced La^{3+} and Ta^{5+} ions into the A/B sites of antiferroelectric $AgNbO_3$, which shifted the electric field-induced antiferroelectric-ferroelectric phase transition to higher fields. The $Ag_{0.94}La_{0.02}Nb_{0.8}Ta_{0.2}O_3$ ceramic achieved a W_{rec} of 6.73 J cm^{-3} and an η of 74.1% under an electric field of 540 kV cm^{-1}. Although higher W_{rec} can be achieved at higher electric field strengths, the contribution of the electric field to polarization is low. It typically requires P_{max} at 400 kV cm^{-1} to achieve 40 μC cm^{-2}. This limitation not only increases the energy loss during the charging process of dielectric capacitors, but also raises the risk and breakdown probability when operating under high electric fields. Additional insulation protection devices and driving instruments need to be applied to the capacitors, anticipating higher working electric field strengths. Therefore, it is necessary to develop dielectric energy storage materials capable of simultaneously achieving high energy density and energy storage efficiency under moderate to low electric fields (< 250 kV cm^{-1}).

In this work, we introduced $NaNbO_3$ (NN) into the $0.8Bi_{0.5}Na_{0.5}TiO_3$–$0.2BaZr_{0.3}Ti_{0.7}O_3$ (BNT–BZT) matrix to construct the (0.8 − *x*)BNT–0.2BZT–*x*NN relaxor ferroelectric ceramics for achieving excellent energy storage behaviors. The design ideas of this work are shown in Fig. 1. The roles of the ferroelectrically active ions Bi^{3+}, Na^+, and Ti^{4+} are to generate locally correlated electric dipoles. The presence of Ba^{2+} and Zr^{4+} with larger ionic radii can expand the [AO_{12}] cube-octahedral and [BO_6] octahedral main frameworks, providing space for ion displacement while partially disrupting the long-range ordered ferroelectric domains.[11,12] The BNT–BZT ceramic exhibits high P_{max}, but the energy storage efficiency is still low due to the large P_r. Upon the introduction of NN, the macroscopic ferroelectric domains will be further disrupted, leading to significant reductions in P_r and the coercive field (E_c). The lone electrons in the outer 5s orbitals of Nb^{5+} and Na^+ can compensate for the polarization loss caused by relaxation.[13] In addition, the large bandgap of NN (~3.58 eV) can enhance the insulation performance of the system, thus improving the E_b.[14] Based on the above composition design, the 0.7BNT–0.2BZT–0.1NN ceramic exhibits weak local correlation but highly extendable unit polarization vectors, demonstrating high P_{max}, extremely low P_r and excellent energy storage performance. It achieves W_{rec} = 3.53 J cm^{-3}, η = 93.5%, and W/E = 160.45 J (kV m^{-2}) under medium–low electric fields (220 kV cm^{-1}).

2. Experimental

Materials preparation: (0.8 − *x*)BNT–0.2BZT–*x*NN (*x* = 0, 0.1, 0.2, and 0.3) ceramics were prepared *via* the conventional solid-state reaction method using Bi_2O_3(99%), Na_2CO_3(99.8%), $BaCO_3$(99%), TiO_2(99%), ZrO_2(99%), and Nb_2O_5(99.5%) as raw materials. The raw materials were first weighed according to the stoichiometric ratio. They were then milled in an attrition mill using anhydrous ethanol as the milling medium for 12 h in a planetary ball mill and dried. Subsequently, the mixed powders were sintered at 850 °C for 4 h, subjected to secondary milling for 12 hours, and dried again. After drying, the powders were thoroughly mixed and ground with a 5 wt% polyvinyl alcohol (PVA) solution. The resulting powder was pressed into discs with a diameter of 8 mm and a thickness of 0.5 mm, followed by sintering. The sintering process involved two steps: 1. Holding at 650 °C for 2 h to remove PVA with a heating rate of 4 °C min^{-1}. 2. Upon completion of removing PVA, ramping up to 1090 °C and holding for 2 h for the final sintering, with a heating rate of 5 °C min^{-1}.

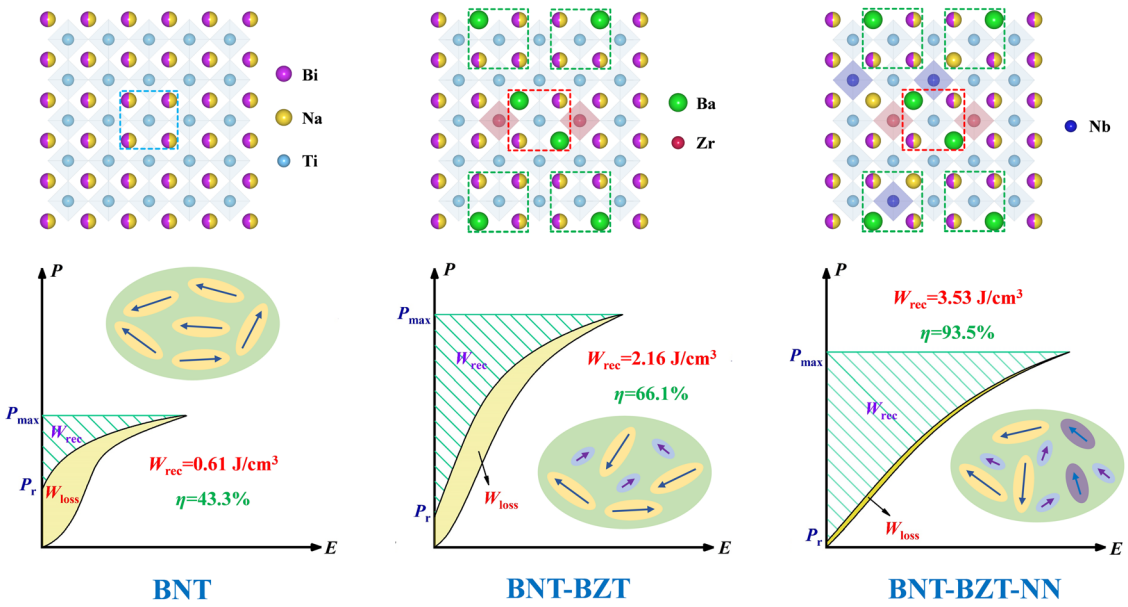

Fig. 1 The design strategy for improving energy storage behaviors of (0.8 − *x*)BNT–0.2BZT–*x*NN ceramics.

Characterization: The crystal structure and phase composition information of $(0.8 - x)$BNT–0.2BZT–xNN ceramics were obtained through X-ray diffraction (XRD, D8 Advanced, Bruker, Germany). The surface morphology images of the samples were photographed using a field emission scanning electron microscope (FESEM, SU8220, Japan). The dielectric properties of the ceramics were measured at different temperatures and frequencies using a Wayne Kerr 6500B system. The room temperature ferroelectric properties (1 Hz, 20 °C), thermal stability (1 Hz, 20–140 °C) and frequency stability (1 Hz–100 Hz, 20 °C) were recorded with a ferroelectric analyzer (TF Analyzer 3000E, Germany).

3. Results and discussion

Fig. 2(a) shows the XRD patterns of $(0.8 - x)$BNT–0.2BZT–xNN ceramics. All ceramic compositions exhibit a single perovskite structure without observable secondary phases, indicating that NN enters the BNT–BZT matrix to form a stable solid solution. As shown in Fig. 2(b), the peak position of the (200) diffraction peak gradually shifts to lower angles with increasing NN content. It is due to the lattice expansion caused by the substitution of Ti^{4+} (0.605 Å, CN = 6) with Nb^{5+} (0.64 Å, CN = 6) with a larger ionic radius.[15,16] The tolerance factor, which measures the stability of the perovskite system, can be calculated using the following equation: $t = \frac{R_A + R_O}{\sqrt{2}(R_B + R_O)}$, where R_A, R_B and R_O represent ionic radii of the A-site, B-site, and oxygen ions, respectively.[17] The tolerance factors of $(0.8 - x)$BNT–0.2BZT–xNN ceramics are 0.9848, 0.9845, 0.9842, and 0.9839, respectively. A decrease in the tolerance factor will cause a change in the direction of close-packed crystal planes for $t < 1$. The larger interstitial sites in the lattice facilitate the occurrence of ion displacement, relaxation behaviors and antiferroelectric distortion.

The surface microstructure images of $(0.8 - x)$BNT–BZT–xNN ceramics are shown in Fig. 3(a)–(d). The grain boundaries of all samples are clear, and the grains are regular and compact with almost no visible pores. Approximately 100 grains are selected for the statistical analysis of the mean grain size, determined using the intercept method, as shown in Fig. 3(e). Initially, with the increase in x, the grain size decreased from 1.09 μm at $x = 0$ to 0.79 μm at $x = 0.1$. It is explained that the substitution of larger ionic radius and atomic weight Nb^{5+} for Ti^{4+} increases the lattice strain energy, and the diffusion coefficient of Nb^{5+} is low, which inhibits crystal growth.[18,19] However, as the NN content further increases, the average grain size increases from 0.79 μm at $x = 0.1$ to 1.23 μm at $x = 0.3$. This phenomenon is closely associated with the defect structure within the ceramic material. The volatilization of Na^+ and Bi^{3+} introduces oxygen vacancies. During the high temperature sintering process, these vacancies facilitate mass transport within the ceramic, resulting in an enlargement of the grain size.[20] High density and low porosity are beneficial for improving the breakdown field strength of the ceramics.

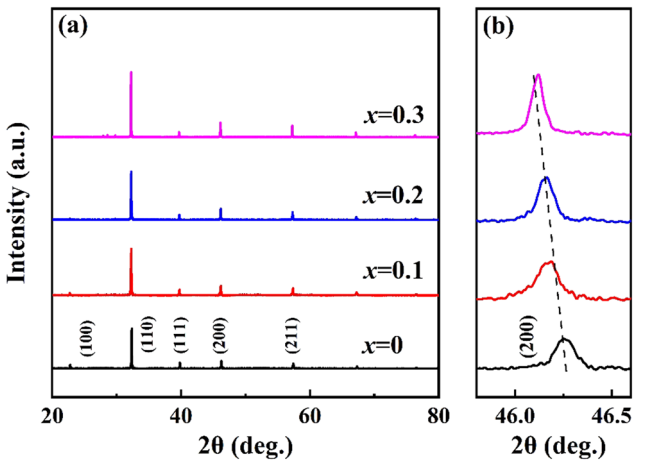

Fig. 2 (a) XRD pattern of $(0.8 - x)$BNT–BZT–xNN ceramics. (b) Partial enlargement of 45.8–46.6°.

Fig. 4(a)–(d) show the temperature-dependent behaviors of the dielectric constants (ε_r) and dielectric losses ($\tan\delta$) of $(0.8 - x)$BNT–BZT–xNN ceramics in the frequency range of 1 kHz to 1 MHz. All samples exhibit characteristics of relaxor behaviors, including diffuse phase transitions and frequency dispersion. In undoped NN samples, two distinct dielectric peaks (T_s) and (T_m) are observed. T_s corresponds to the thermal evolution of discrete polar nanoregions, while T_m corresponds to the phase transition from rhombohedral to tetragonal phases.[21] With the addition of NN, the T_s peaks significantly shift towards lower temperatures, corresponding to approximately 87.6 °C, 51.5 °C, and 20 °C, while the T_m peaks disappear. This phenomenon can be attributed to the stabilization of the *P4bm* polar nanoregions (PNRs) at high temperatures, leading to the observation of only low-temperature T_s anomaly transition peaks in the ε_r-T curves.[22] Similar features were also observed in other BNT-based ceramics modified with $NaNbO_3$, $CaZrO_3$, and $NbTaO_3$.[23–25] It is noteworthy that the weak peaks (T_c) appear in the high-temperature region [Fig. 4(b)–(d)], which is attributed to the contribution of the NN antiferroelectric phase.[26] The ε_r gradually decreases with the increase in NN content. It can be explained by the increased compositional disorder, diffusion of polar nanoregions, and reorientation of ferroelectric domains, resulting in a dilution effect.[27] Furthermore, all samples exhibit relatively low dielectric losses (<0.15) from 20 °C to 450 °C, indicating their strong insulation capability over a wide temperature range.

In order to evaluate the ferroelectric properties of $(0.8 - x)$BNT–BZT–xNN ceramics, Fig. 5(a) and (b) illustrate the biaxial P–E loops and variations of important parameters at 100 kV cm^{-1}. The sample with $x = 0$ exhibits the highest P_{max} and ΔP. However, this composition exhibits strong hysteresis and saturation polarization tendencies, which are not suitable for energy storage. After the introduction of NN, the P–E loops exhibit a more elongated and linear shape. These elongated P–E loops can reduce polarization losses during charging and discharging processes, thereby increasing energy storage density. Both P_{max} and ΔP (P_{max}–P_r) gradually decrease with

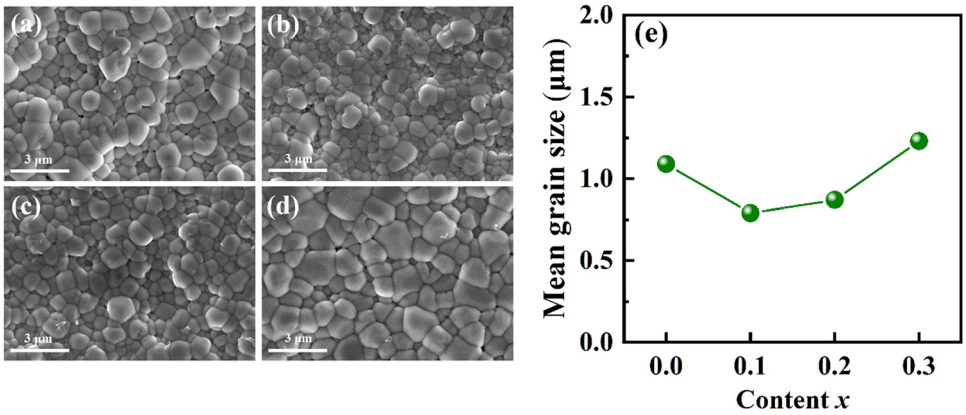

Fig. 3 (a)–(d) SEM images and (e) mean grain size with the increase of content x of (0.8 − x)BNT–BZT–xNN ceramics.

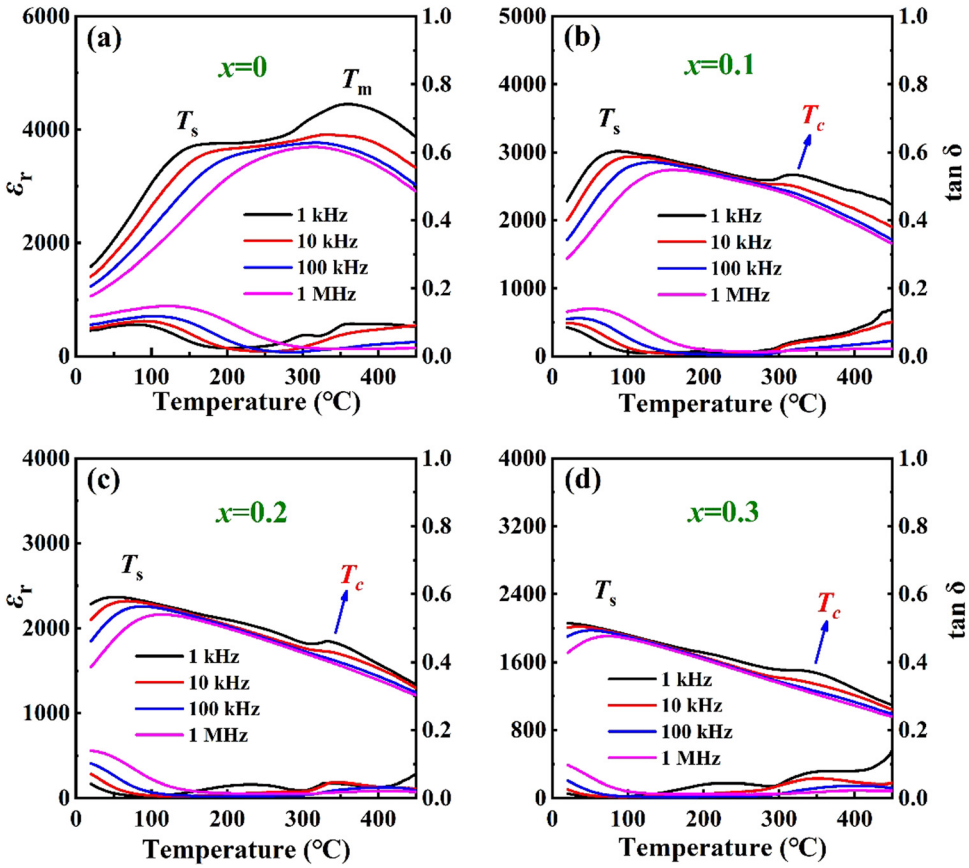

Fig. 4 (a)–(d) Temperature dependence of ε_r and tan δ of (0.8 − x)BNT–BZT–xNN ceramics at different frequencies.

increasing x content, while P_r decreases initially and then stabilizes. These results are consistent with the observations from the ε_r–T curves, attributed to the disruption of partial long-range order in the system by A-site Na^+ and B-site Nb^{5+}, thereby increasing the relaxor behaviors of ceramics. The formation of polar nanoregions is facilitated by the presence of local disorder, and the recovery of ferroelectric domains to their initial orientations upon the removal of external electric fields is made easier by the existence of local random electric fields. Furthermore, the gradual increase in the content of the weakly polar *P4bm* phase, along with these factors, collectively contributes to the decrease in both P_{max} and P_r.

Fig. 6(a) displays the unipolar P–E loops of (0.8 − x)BNT–BZT–xNN ceramic samples under critical electric fields, in order to comprehensively evaluate their energy storage performance. It is obvious that the curvature of the P–E loops decreases with an increase in the NN content due to the delayed saturation of polarization saturation. For samples with NN

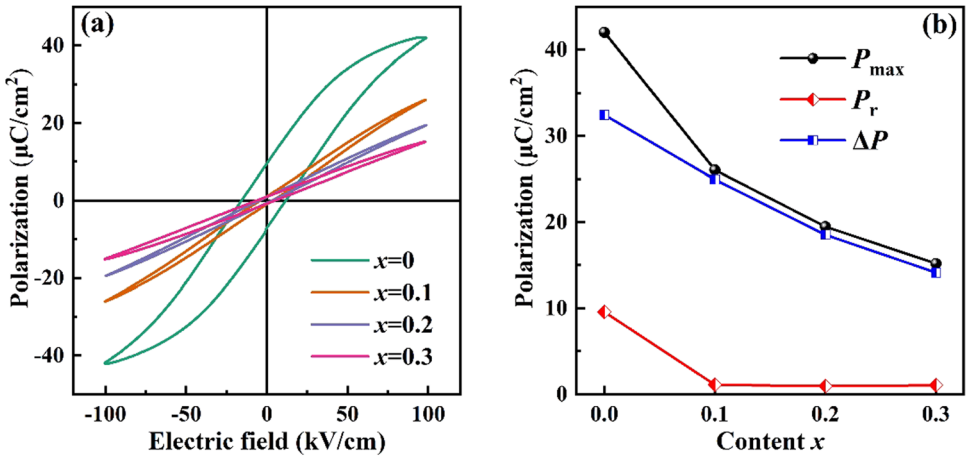

Fig. 5 (a) The bipolar *P*–*E* loops at 100 kV cm^{-1} of (0.8 − *x*)BNT–BZT–*x*NN ceramics and (b) P_{max}, P_r and ΔP (P_{max}–P_r) as a function of *x* content.

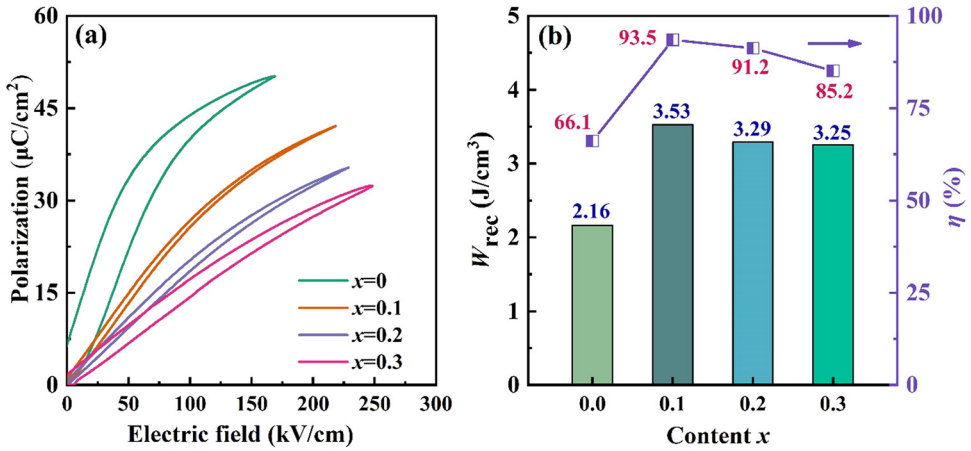

Fig. 6 (a) Unipolar *P*–*E* loops at critical electric fields of (0.8 − *x*)BNT–BZT–*x*NN ceramics and (b) W_{rec} and η are calculated from (a).

content ranging from 0 to 0.3, the E_b is measured to be 170, 220, 230 and 250 kV cm^{-1}, respectively. As expected, NN widened the bandgap of the system and improved its insulating properties, resulting in an enhanced E_b. The values for W_{rec} and η of (0.8 − *x*)BNT–BZT–*x*NN ceramics were calculated from the unipolar *P*–*E* loops and are presented in Fig. 6(b). The W_{rec} and η increased from 2.16 J cm^{-3} and 66.1% for x = 0 to 3.53 J cm^{-3} and 93.5% for x = 0.1, respectively, resulting in a percentage change of 63.4% and 41.5%, respectively. However, W_{rec} and η slightly decreased with the further increase in x. This decrease is primarily attributed to the enhancement of relaxor behaviors and the merging of domain switching caused by the reinforcement of antiferroelectric phases. The delay of polarization saturation, the improvement of relaxation and the increase in E_b significantly enhance the energy storage capability of (0.8 − *x*)BNT–BZT–*x*NN ceramics.

Fig. 7(a)–(f) show the unipolar *P*–*E* loops, W_{rec}, and η of (1 − *x*)BNT–BZT–*x*NN ceramics (x = 0–0.2) under different electric fields. The overall shape of the *P*–*E* loops for all samples remained unchanged as the electric field increased, while W_{rec} almost linearly increased with the electric field. In the sample with x = 0, P_{max} increased from 11.6 μC cm^{-2} at 30 kV cm^{-1} to 50.2 μC cm^{-2} at 170 kV cm^{-1}. Owing to the presence of Ba^{2+} and Zr^{4+} with large ionic radii, the octahedral framework is expanded and sufficient space is provided for ion displacement, thus enabling a significant P_{max} to be achieved even at lower electric field. Although moderate W_{rec} (∼2.16 J cm^{-3}) was achieved in the 0.8BNT–0.2BZT ceramic, due to the low η (∼66.1%), it is still not suitable for energy storage in dielectric capacitors. Consistent with the intended design of this work, the incorporation of NN has enhanced relaxation and compensated for polarization losses, while exhibiting high local polarity. Thus, the sample with x = 0.1 exhibits a large P_{max} (∼42.1 μC cm^{-2}) at 220 kV cm^{-1}, a small P_r (∼1.1 μC cm^{-2}), high W_{rec} (∼3.53 J cm^{-3}), η (∼93.5%), and W_{rec}/E (∼160.45 J (kV m^{-2})). Interestingly, η shows almost no dependence on the electric field, with a variation rate of less than 0.7%. It indicates that the η of 0.7BNT–0.2BZT–0.1NN ceramic has outstanding electric field stability. In the sample with x = 0.2, due to the enhancement of relaxation and antiferroelectricity, polar domains grow

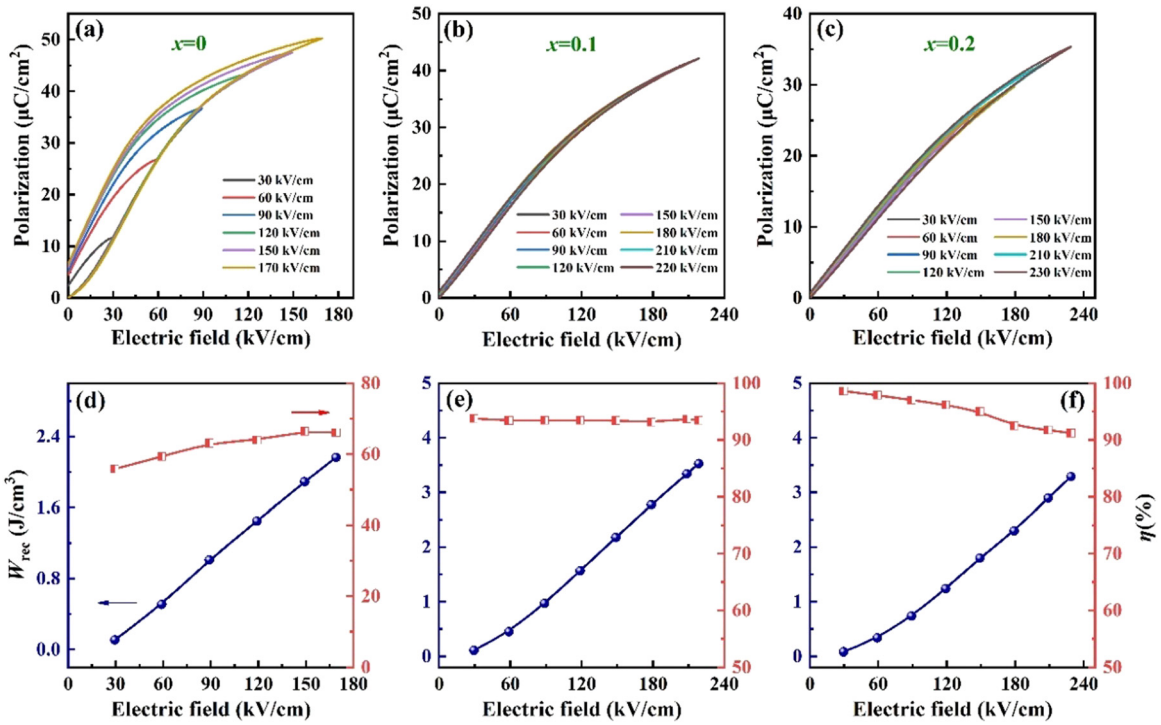

Fig. 7 (a)–(c) Unipolar *P*–*E* loops under different electric fields, and (d)–(f) electric-field dependence of W_{rec} and η.

and merge under higher electric fields, leading to slightly lower W_{rec} and η compared to the sample with x = 0.1. Furthermore, a comparison with recent reported work on lead-free ceramic energy storage properties is presented in Table 1.[8,23,27–37] Our work is very significant as it not only maintains higher W_{rec} and η, but also has a leading W_{rec}/E under a low electric field. (1 − x)BNT–BZT–xNN ceramics will shine in future energy storage components of power systems.

Components used for pulse energy storage inevitably generate heat during operation and need to work in some harsh environments. Therefore, the temperature and frequency stability of dielectric energy storage ceramics are crucial in practical applications. Fig. 8(a) shows the *P*–*E* loops of the 0.7BNT–0.2BZT–0.1NN ceramic at different temperatures at 150 kV cm^{-1}. Fig. 8(b) summarizes the changes in energy storage parameters. As the temperature increases, W_{rec} and η initially increase slightly and then decrease. It can be attributed to the increase in weakly polar phases, which leads to a slight increase in W_{rec} and η due to the decrease in P_{max} and P_r. As the temperature continues to rise, P_{max} further decreases along with an increase in P_r and leakage current, causing W_{rec} and η to decrease (see the inset of Fig. 8(a)). Within the range of 20–140 °C, W_{rec} only decreases by 7.2%, and η remains above 90%. The energy storage performance of 0.7BNT–0.2BZT–0.1NN ceramics at different frequencies under 120 kV cm^{-1} is shown in Fig. 8(c) and (d). The shape of the *P*–*E* loops remains unchanged at different frequencies. With increasing test frequency, the ferroelectric domains cannot respond in time, so W_{rec} and η gradually decrease. The sample only experiences a 5.3% decrease in W_{rec} and maintains η of over 85% at frequencies ranging from 1 to 100 Hz. In conclusion,

Table 1 A comparison of the energy storage behaviors between this work and other reported lead-free ceramics in recent years

Composition	W_{rec} (J cm^{-3})	η (%)	E (kV cm^{-1})	W_{rec}/E J (kV m^{-2})	Ref.
$0.7Na_{0.5}Bi_{0.5}TiO_3$–$0.3NaNbO_3$: 7%$CaZr_{0.5}Ti_{0.5}O_3$	4.93	93.3	410	120.24	8
$0.8(0.94Na_{0.5}Bi_{0.5}TiO_3$–$0.06BaTiO_3)$–$0.2Bi(Mg_{2/3}Nb_{1/3})O_3$	1.88	82.15	150	125.33	27
$Bi_{0.395}Na_{0.325}Sr_{0.245}TiO_3$–$Ca_{0.7}La_{0.2}TiO_3$	8.30	80	660	125.76	28
$0.94(Na_{0.88}Sm_{0.04}NbO_3)$–$0.06(BiFeO_3)$	4.00	80	460	86.96	29
$0.875K_{0.5}Na_{0.5}NbO_3$–$0.125Bi(Sr_{0.5}Zr_{0.5})O_3$	2.95	84	245	120.41	23
$0.925(K_{0.5}Na_{0.5})NbO_3$–$0.075Bi(Zn_{2/3}(Ta_{0.5}Nb_{0.5})_{1/3}O_3)$	4.05	87.4	307	131.92	30
Mn-$0.97AgNbO_3$–$0.03Bi_{0.5}Na_{0.5}TiO_3$	3.40	62	220	154.55	31
$0.85K_{0.5}Na_{0.5}NbO_3$–$0.15Bi(Zn_{2/3}Ta_{1/3})O_3$	6.70	92	600	111.67	32
$0.925Ba_{0.85}Ca_{0.15}Zr_{0.1}Ti_{0.9}O_3$–$0.025BiMg_{2/3}Nb_{1/3}O_3$	3.81	90.5	405	94.07	33
$0.7(Bi_{0.47}La_{0.03}Na_{0.5})_{0.94}Ba_{0.06}TiO_3$–$0.3SrTi_{0.875}Nb_{0.1}O_3$	4.2	89.3	380	110.53	34
$0.82NaNbO_3$–$0.18Ba(Fe_{0.5}Nb_{0.5})O_3$	3.55	84.1	450	78.89	35
$0.8Na_{0.5}Bi_{0.5}TiO_3$–$0.2Sm_{1/3}Sr_{1/2}(Mg_{1/3}Nb_{2/3})O_3$	7.3	78.2	480	152.08	36
$0.9(0.6Bi_{0.5}Na_{0.5}TiO_3$–$0.4Sr_{0.7}Bi_{0.2}TiO_3)$–$0.1SmFeO_3$	7.2	86	430	167.44	37
$0.7Bi_{0.5}Na_{0.5}TiO_3$–$0.2BaZr_{0.3}Ti_{0.7}O_3$–$0.1NaNbO_3$	3.53	93.5	220	160.45	This work

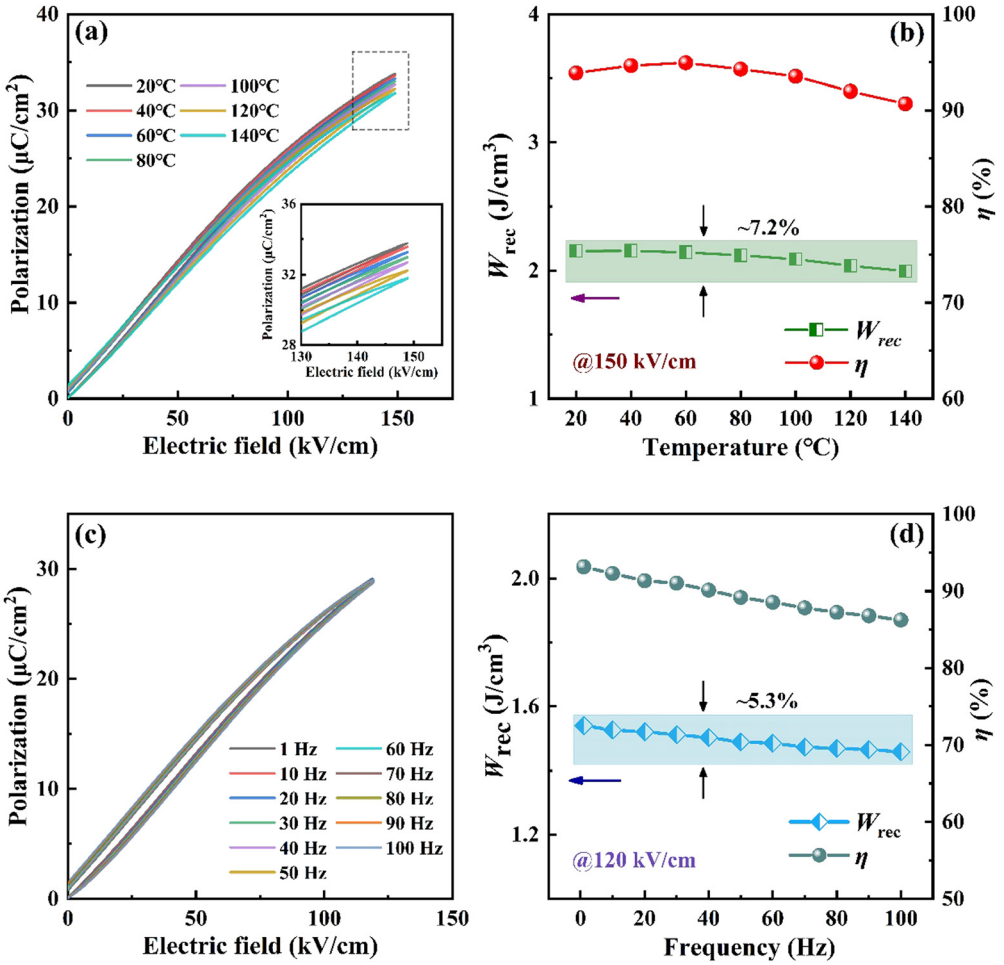

Fig. 8 Unipolar *P*–*E* loops and energy storage properties of 0.7BNT–0.2BZT–0.1NN ceramic at (a) and (b) different temperatures and (c) and (d) different frequencies. The inset in (a) shows a localized magnified view of P_{max}.

0.7BNT–0.2BZT–0.1NN ceramics exhibit excellent thermal/frequency stability, making them an ideal candidate material for high-performance ceramic capacitors.

4. Conclusions

In summary, we have successfully synthesized $(0.8 - x)$BNT–0.2BZT–xNN relaxor ferroelectric ceramics with desirable energy storage behaviors using a solid-state reaction method. The regulation of key factors influencing energy storage properties, such as the dielectric relaxation behaviors and E_b of ceramics, has been significantly improved based on component design. The addition of NN to BNT–BZT results in an unordered polarization local structure with alternating weak and strong polar clusters, resulting in high P_{max} and low P_r at the macroscopic level. The 0.7BNT–0.2BZT–NN ceramic exhibits excellent W_{rec} ($\sim$3.53 J cm^{-3}), ultra-high η ($\sim$93.5%) and leading W_{rec}/E ($\sim$160.45 J (kV m^{-2})) at 220 kV cm^{-1}. In addition, this ceramic shows outstanding electric field stability (30–220 kV cm^{-1}, $\Delta\eta < 0.7\%$), thermal stability (20–140 °C, $\Delta W_{rec} < 7.2\%$), and frequency stability (1–100 Hz, $\Delta W_{rec} < 5.3\%$). These results suggest that the 0.7BNT–0.2BZT–NN ceramic has great potential for application in advanced pulsed power systems.

Author contributions

Jian Yang: writing – original draft preparation, data curation, methodology, conceptualization and supervision. Xiaolong Zhu: investigation, methodology, and writing – reviewing and editing. Haotian Wang: formal analysis and writing – reviewing and editing. Yixiao Zhang: writing – reviewing and editing. Pengfei Guan: methodology validation and writing – review and editing. Shiguang Yan: resources. Ming Zheng: formal analysis, methodology, funding acquisition, and writing – reviewing and editing.

Data availability

The data that support the findings of this study are available from the corresponding author upon reasonable request.

Conflicts of interest

There are no conflicts to declare.

Acknowledgements

This work was supported by the National Natural Science Foundation of China (grant no. 12004423), the Opening Project of Key Laboratory of Inorganic Functional Materials and Devices, Chinese Academy of Sciences (grant no. KLIFMD202303), and the Materials Science and Engineering Discipline Guidance Fund of China University of Mining and Technology (grant no. CUMTMS202201).

References

1 L. T. Yang, X. Kong, F. Li, H. Hao, Z. X. Cheng, H. X. Liu, J. F. Li and S. J. Zhang, *Prog. Mater. Sci.*, 2019, **102**, 72–108.
2 G. Wang, Z. L. Lu, Y. Li, L. H. Li, H. F. Ji, A. Feteira, D. Zhou, D. W. Wang, S. J. Zhang and I. M. Reaney, *Chem. Rev.*, 2021, **121**, 6124–6172.
3 C. W. Sun, J. A. Alonso and J. J. Bian, *Adv. Energy Mater.*, 2021, **11**, 2000459.
4 X. H. Fan, J. Wang, H. Yuan, Z. H. Zheng, J. Zhang and K. J. Zhu, *J. Adv. Ceram.*, 2023, **12**, 649–680.
5 H. Pan, F. Li, Y. Liu, Q. H. Zhang, M. Wang, S. Lan, Y. P. Zheng, J. Ma, L. Gu, Y. Shen, P. Yu, S. J. Zhang, L. Q. Chen, Y. H. Lin and C. W. Nan, *Science*, 2019, **365**, 578–582.
6 X. P. Zhu, Y. F. Gao, P. Shi, R. R. Kang, F. Kang, W. J. Qiao, J. Y. Zhao, Z. Wang, Y. Yuan and X. J. Lou, *Nano Energy*, 2022, **98**, 107276.
7 Z. Y. Che, L. Ma, G. G. Luo, C. Xu, Z. Y. Cen, Q. Feng, X. Y. Chen, K. L. Ren and N. N. Luo, *Nano Energy*, 2022, **100**, 107484.
8 Y. Chen, Y. Huang, Y. D. Zuo, H. S. Wang, K. Liu, B. Y. Fan, Q. F. Zhang, G. Z. Zhang, S. L. Jiang and M. Shen, *J. Eur. Ceram. Soc.*, 2022, **42**, 6985–6996.
9 X. Z. Zhang, P. Zheng, L. L. Li, F. Wen, W. F. Bai, J. J. Zhang, L. Zheng and Y. Zhang, *Scr. Mater.*, 2022, **211**, 114514.
10 B. Y. Li, Z. N. Yan, X. F. Zhou, H. Qi, V. Koval, X. G. Luo, H. Luo, H. X. Yan and D. Zhang, *ACS Appl. Mater. Interfaces*, 2023, **15**, 4246–4256.
11 H. Liu, Z. Sun, J. Zhang, H. Luo, Y. Zhang, A. Sanson, M. Hinterstein, L. Liu, J. C. Neuefeind and J. Chen, *J. Am. Chem. Soc.*, 2024, **146**, 3498–3507.
12 I. Levin, W. J. Laws, D. Wang and I. M. Reaney, *Appl. Phys. Lett.*, 2017, **111**, 212902.
13 W. J. Shi, Y. L. Yang, L. Y. Zhang, R. Y. Jing, Q. Y. Hu, D. O. Alikin, V. Y. Shur, J. H. Gao, X. Y. Wei and L. Jin, *Ceram. Int.*, 2022, **48**, 6512–6519.
14 Y. Ning, Y. Pu, C. Wu, S. Zhou, L. Zhang, J. Zhang, X. Zhang and Y. Shang, *J. Mater. Sci. Technol.*, 2023, **145**, 66–73.
15 Y. Zhang, A. W. Xie, J. Fu, X. W. Jiang, T. Y. Li, C. Zhou and R. Z. Zuo, *ACS Appl. Mater. Interfaces*, 2022, **14**, 40043–40051.
16 Z. C. Liu, P. R. Ren, C. B. Long, X. Wang, Y. H. Wan and G. Y. Zhao, *J. Alloys Compd.*, 2017, **721**, 538–544.
17 Y. Yin, J. R. Yu, Y. C. Tang, A. Z. Song, H. Liu, D. Yang, J. F. Li, L. Zhao and B. P. Zhang, *J. Materiomics*, 2022, **8**, 611–617.
18 K. Y. Wang, W. H. Li, R. K. Zhao, X. G. Tang, S. Y. Zhang, Y. S. Zhang, J. Hu, Z. H. Shen, Y. P. Jiang and X. B. Guo, *Ceram. Int.*, 2024, **50**, 5276–5284.
19 X. Qiao, D. Wu, F. Zhang, M. Niu, B. Chen, X. Zhao, P. Liang, L. Wei, X. Chao and Z. Yang, *J. Eur. Ceram. Soc.*, 2019, **39**, 4778–4784.
20 X. B. Zhang, G. S. Chen, Z. X. Liu, X. L. Miao, Z. H. Zhang, D. Y. Chen, K. H. Lam, M. Zeng, X. S. Gao and J. M. Liu, *Chem. Eng. J.*, 2024, **480**, 147973.
21 C. B. Long, Z. Q. Su, H. M. Song, A. W. Xu, L. J. Liu, Y. Li, K. Zheng, W. Ren, H. J. Wu and X. D. Ding, *Energy Storage Mater.*, 2024, **65**, 103055.
22 W. X. Jia, Y. D. Hou, M. P. Zheng and M. K. Zhu, *J. Alloys Compd.*, 2017, **724**, 306–315.
23 W. X. Luo, M. X. Wu, Y. F. Han, X. Zhou, L. J. Liu, Q. W. He, P. R. Ren, H. M. Yang, H. Yang, Q. Wang, Z. H. Chen, X. H. Liang and Z. F. Chen, *J. Am. Ceram. Soc.*, 2023, **106**, 4723–4731.
24 M. Acosta, J. D. Zang, W. Jo and J. Rödel, *J. Eur. Ceram. Soc.*, 2012, **32**, 4327–4334.
25 Q. Xu, H. X. Liu, L. Zhang, J. Xie, H. Hao, M. H. Cao, Z. H. Yao and M. T. Lanagan, *RSC Adv.*, 2016, **6**, 59280–59291.
26 Z. Y. Liu, H. Q. Fan, J. S. Lu, Y. Q. Mao and Y. Zhao, *J. Eur. Ceram. Soc.*, 2018, **38**, 2871–2878.
27 Z. Li, J. Y. Zhang, C. B. Wang, Z. X. Wang, N. N. Lei, L. F. Zheng, D. J. Long, X. T. Wei, J. Zhang, Z. Wang, X. Yan, T. Ai, D. W. Wang and Y. H. Niu, *Ceram. Int.*, 2023, **49**, 38735–38742.
28 L. M. Tang, Z. Y. Yu, Z. B. Pan, J. H. Zhao, Z. Q. Fu, X. Q. Chen, H. H. Li, P. Li, J. J. Liu and J. W. Zhai, *Small*, 2023, **19**, 2302346.
29 X. J. Meng, Z. Y. Yang, Y. Yuan, B. Tang and S. R. Zhang, *Chem. Eng. J.*, 2023, **477**, 147097.
30 X. Z. Wang, Y. Huan, P. Y. Zhao, X. M. Liu, T. Wei, Q. W. Zhang and X. H. Wang, *J. Materiomics*, 2021, **7**, 780–789.
31 Y. H. Xu, Y. Guo, Q. Liu, G. D. Wang, J. L. Bai, J. J. Tian, L. Lin and Y. Tian, *J. Eur. Ceram. Soc.*, 2020, **40**, 56–62.
32 D. Li, D. Zhou, D. Wang, W. C. Zhao, Y. Guo and Z. Q. Shi, *Adv. Funct. Mater.*, 2022, **32**, 2111776.
33 Z. H. Dai, J. L. Xie, Z. B. Chen, S. Zhou, J. J. Liu, W. G. Liu, Z. Z. Xi and X. B. Ren, *Chem. Eng. J.*, 2021, **410**, 128341.
34 L. K. Wu, L. M. Tang, Y. Z. Zhai, Y. L. Zhang, J. J. Sun, D. Hu, Z. B. Pan, Z. Su, Y. Zhang and J. J. Liu, *J. Materiomics*, 2022, **8**, 537–544.
35 G. F. Liu, L. Chen, H. F. Yu, Z. F. Zhang, J. Wu, C. Zhou, H. Qi and J. Chen, *Chem. Eng. J.*, 2023, **474**, 145705.
36 Q. Zheng, B. Xie, Y. Tian, Q. Wang, H. Luo, Z. Liu and H. Zhang, *J. Materiomics*, 2023, DOI: 10.1016/j.jmat.2023.10.005.
37 Q. Zheng, B. Xie, Q. Wang, F. Xue, K. Guo, Z. Liu, P. Mao, W. Cao, H. Luo and H. Zhang, *Chem. Eng. J.*, 2024, **483**, 149154.

